Computing resolution for neuromagnetic imaging systems

Kensuke Sekihara

Department of Advanced Technology in Medicine
Tokyo Medical and Dental University
1-5-45 Yushima, Bunkyo-ku, Tokyo 113-8519, Japan

Signal Analysis Inc.
Hachioji, Tokyo 192-0031, Japan

Abstract

This paper proposes a novel signal-detection-theory-based definition for the resolution of neuromagnetic imaging systems, and develops a Monte Carlo computer simulation method to compute the resolution. Using the resolution as a performance measure, the performance of various types of sensor hardware is assessed. The assessments include performance improvements due to the increase in the number of sensors and performance changes due to the change in the gradiometer baseline or change in the helmet size. We compare the performance difference between planar and axial gradiometer arrays, and also compare the performance between the conventional radial sensor array and a vector sensor array. We compute the resolution of two existing neuromagnetic sensor arrays, MEGvision$^{\mathrm{TM}}$ (Yokogawa Electric Corporation, Tokyo, Japan) and Elekta-Neuromag TRIUX$^{\mathrm{TM}}$ (Elekta Corporate, Stockholm, Sweden).

1 Introduction

Electrophysiological activity of neurons in the cerebral cortex generates tiny magnetic fields outside the scalp. Direct non-invasive measurements of this neuronal activity on a sub-millisecond time scale can be achieved by magnetoencephalography (MEG)[1][2]. Modern MEG systems are capable of whole-head coverage with simultaneous measurements by nearly 300 sensors. Such whole-head sensor arrays, together with advanced signal processing algorithms, now enable imaging of dynamic brain activity – referred to as neuromagnetic imaging[3][4][5].

One problem with neuromagnetic imaging is that no clear measure exists for assessing the overall performance of imaging systems. A naive (but very popular) index used for assessing the performance of neuromagnetic imaging systems is the number of sensors. Although one can imagine that a system with larger number of sensors should have better performance than that of a system with smaller number of sensors, it has been difficult to quantitatively assess the performance improvements due to increasing the number of sensors.

Theoretical assessments of the performance of MEG multi-channel sensor systems have been proposed that apply an information theoretic approach to the sensor data[6]. It may be true that a sensor array that captures a greater amount of information gives higher-quality source images. However, since a quantitative relationship between the information content captured in sensor data and the quality of source images is unknown, such an information theoretic analysis on the sensor data is insufficient for quantitative performance assessments of neuromagnetic imaging systems.

Resolution expresses a system's capability to discriminate two closely located sources and has conventionally been used to assess the performance of a wide variety of imaging systems, from classic optical instruments to medical imaging systems including X-ray computed tomography(CT) and magnetic resonance imaging(MRI). However, it is difficult to define the resolution of neuromagnetic imaging systems because this capability depends on the location and orientation of sources because of the space-variant nature of this imaging method.

Therefore, to assess the resolution of neuromagnetic imaging systems, some type of Monte Carlo-based method is needed in which the source locations and orientations are randomly chosen in each Monte Carlo trial. This paper develops such a Monte Carlo-based method, which incorporates a novel definition of resolution computed based on the results from Monte Carlo experiments.

Using the resolution, we can explore the relationship between the system's performance and choices of various hardware design parameters. We can make a quantitative comparison among existing sensor systems and predict the performance of future systems. In Section 2, we describe, in detail, how the resolution for neuromagnetic imaging systems is defined and computed. Using the resolution as a performance measure, we compare various types of sensor hardware in Section 3. We also compare the resolution of two existing neuromagnetic imaging systems, MEGvision$^{\mathrm{TM}}$ (Yokogawa Electric Corporation, Tokyo, Japan) and Elekta-Neuromag TRIUX$^{\mathrm{TM}}$ (Elekta Corporate, Stockholm, Sweden).

2 Monte Carlo method for computing spatial resolution

2.1 Sensor data generation

We have developed a Monte Carlo simulation method to compute the resolution of neuromagnetic imaging systems. In this method, we assume two sources that have equal intensity. The locations and orientations of the two sources are randomly chosen in each Monte Carlo trial, with the distance of the sources Δ fixed across all trials. The locations of the two sources are confined within the simulated brain region shown in Fig. 1. A spherical-shell region with outer radius 8cm and inner radius 1cm is defined as the brain region and the region more than 4cm below the sphere center is excluded. The center of the brain region is 10.5 cm below the sensor located at the center of the sensor array.

The two sources have random time courses generated using Gaussian random numbers; the time courses have 4000 time points. One hundred Monte Carlo trials of simulated sensor data are generated, each with random source locations and orientations with a fixed inter-source distance. Gaussian white noise is added to this signal magnetic field to generate the simulated sensor data. The standard deviation of the sensor noise is fixed to 50 fT throughout the computer simulation in this study[1]. A two-orientation forward lead field is calculated using the single spherical-shell model[7], and to compute the signal magnetic field, the source activity is projected to the sensor space through the lead field.

---

[1] The rationale for this 50 fT value is as follows: Modern SQUID-based biomagnetometers typically have the noise level of 5 $\mathrm{fT}/\sqrt{\mathrm{Hz}}$, so if we assume the bandwidth of the measurement to be 100 Hz, then the measured data contain a noise level of 50 fT.

2.2 Source reconstruction and local peak detection

The simulated brain volume in Fig. 1 is segmented into voxels. In our computer simulation, the voxel size V is determined according to the inter-source distance, such that

$$V = 0.2\mathit{\Delta} \qquad \mathit{\Delta} \leq 2.5 \text{ cm}, \tag{1}$$

$$V = 0.5 \text{ cm} \qquad \mathit{\Delta} > 2.5 \text{ cm}. \tag{2}$$

The rationale for determining the voxel size in this manner is given in the Appendix. Adaptive beamformer source reconstruction[4][8] is performed and a source power map (the power of the time courses at each voxel) is computed at all voxel locations. The localization accuracy is then assessed in the following manner.

If a voxel has a value higher than its nearest neighbors in three dimensions, we determine that a "local peak" exists at that voxel. After all the local peak locations are searched, we test whether each local peak is within a particular distance D from one of the true source locations. If a particular peak is within D from a true source location, that peak is labeled as a "detected source". If there is no true source within D from the local peak, that local peak is labeled a "false detection". In our computer simulation, the distance D is referred to as the detection radius. Using the voxel size V, the detection radius is set such that

$$D = 1.5V. \tag{3}$$

The rationale for determining D in this way is presented in the Appendix.

2.3 A-prime metric

Capability for detecting sources is assessed using a signal-detection-theory-based metric called the A-prime metric[9]. To compute the A-prime metric, we first compute the hit rate H, which is a ratio describing the correct source detections. We define the numbers of detected sources n_D and undetected sources n_U. Using the relationship $n_D + n_U = 2$ where 2 is the total number of true sources, the hit rate H is computed by

$$H = \langle \frac{n_D}{n_D + n_U} \rangle = \frac{\langle n_D \rangle}{2}, \tag{4}$$

where $\langle \cdot \rangle$ indicates averaging across all Monte Carlo trials.

Defining the number of false detections in each Monte Carlo trial as n_F, we compute the false-detection rate F as follows:

$$F = \langle \frac{n_F}{n_D + n_F} \rangle = \langle \frac{n_F}{n_L} \rangle, \tag{5}$$

where n_L is the number of total local peaks in each Monte Carlo trial, and the relationship $n_L = n_D + n_F$ is used[2]. Once H and F are obtained, we can

---

[2] The definition of the false-detection rate above differs from that used in [10], where F is obtained using $F = n_F/(\text{maximum number of } n_F)$ and the resultant F becomes significantly different than that calculated using Eq. (5) when the signal-to-ratio (SNR) is low.

compute the A-prime metric, A_p, which is equal to the area under the receiver operating characteristics (ROC) curve for H versus F. Since we have only a single pair of H and F, the first-order approximation is given by

$$A_p = \frac{H - F}{2} + \frac{1}{2}. \tag{6}$$

The above equation is derived in the Appendix. It should be noted that the A-prime metric was used to evaluate the performance of source reconstruction algorithms in previous studies[10][11][12].

2.4 Spatial resolution

The spatial resolution is generally defined as the minimum distance at which the two sources are separately detected. In our Monte Carlo computer simulation, the A-prime metric is obtained for two sources with a fixed inter-source distance. We repeat the Monte Carlo simulation with different inter-source distances and plot the A-prime metric versus the inter-source distance.

We then look for the source distance that gives the A-prime metric equal to a certain value α ($0.5 \leq \alpha \leq 1$), and define this source distance to be the spatial resolution of the imaging system for a given source intensity. By repeating the whole procedure with various source intensities, we obtain a plot of resolution versus source intensity, which represents the resolution of the imaging system under assessment.

2.5 Error-bar estimation using bootstrap method

To obtain the confidence interval of the spatial resolution, we use the bootstrap method. Denoting the number of Monte Carlo trials as M, we have M results for n_D and n_F, which are denoted $n_D^1, \ldots, n_D^M$ and $n_F^1, \ldots, n_F^M$. In the bootstrap method, we first choose M bootstrap samples from $n_D^1, \ldots, n_D^M$ with replacements, and the bootstrap samples are denoted $\widetilde{n}_D^1, \ldots, \widetilde{n}_D^M$. We then compute the bootstrap hit rate $\widetilde{H}$. We also compute the bootstrap false detection rate $\widetilde{F}$ using bootstrap samples $\widetilde{n}_F^1, \ldots, \widetilde{n}_F^M$ taken from $n_F^1, \ldots, n_F^M$ with replacements.

We can now compute the bootstrap A-prime using $\widetilde{H}$ and $\widetilde{F}$, and we plot the bootstrap A-prime versus the inter-source distance. The resolution, which is the inter-source distance that gives the A-prime equal to α, is finally obtained. Since there are many ways to choose the bootstrap samples, we can obtain the bootstrap distribution of the estimated resolution and finally obtain the confidence interval of the estimated resolution values by using the bootstrap distribution. We set error bars to the 95% confidence interval in this paper.

3 Results of computing resolution for various types of neuromagnetic imaging systems

3.1 Resolution computation

We assume four types of sensor arrays having 80, 160, 320, and 640 sensors for resolution assessment experiments. In these sensor arrays, sensors are aligned on a surface of a spherical helmet that has a 13 cm radius. The sensor locations of these four types of sensor arrays are shown in Fig. 2. As shown here, three-quarters of the helmet surface are covered by sensors, which are arranged with an equal inter-sensor spacing. In our experiments, the sensor is a first-order axial gradiometer with a 5 cm baseline unless otherwise noted.

We perform the Monte Carlo computer simulation described in the preceding section. Two sets of source reconstruction results are shown as examples in Fig. 3. For these results, the two sources are 3 cm apart, and the sensor system with 160 sensors is assumed. Here, Fig. 3(a) shows a fairly high signal-to-noise ratio (SNR)[3] case (SNR of 2) in which the two sources are detected. A low SNR case (SNR of 0.5) in which the two sources are not resolved is shown in Fig. 3(b). Obviously, the A-prime metric is equal to one in the first case. It is equal to zero in the second case since the hit rate is zero and the false detection rate is one.

By performing the Monte Carlo experiments with various inter-source distances, the dependence of the A-prime metric on the inter-source distance is obtained. Examples of plotting the three metrics, namely the hit rate, the false detection rate, and the A-prime metric, with respect to the inter-source distance are shown in Fig. 4. The results in Fig. 4(a) are obtained using the source intensity set to 60 nAm, which gives an average SNR of 3. In this figure, we can see a clear tendency that the hit rate increases, the false-detection rate decreases, and the resultant A-prime metric increases as the inter-source distance increases.

In our computer simulation, the resolution is defined as the inter-source distance that gives an A-prime metric of 0.75. In Fig. 4, the level of $A_p = 0.75$ is shown by a horizontal broken line, and the vertical broken line indicates the resolution, which is the inter-source distance giving $A_p = 0.75$. The plot in Fig. 4(a) shows that the resolution in this case is slightly larger than 2 cm and, using the interpolation, the resolution is computed to be 2.1 cm.

The results in Fig. 4(b) show an example for a case where the resolution is undefined because the value of A-prime never reaches 0.75, even when the inter-source distance is as large as 6 cm. These plots were obtained with a source intensity of 6 nAm, which gives an average SNR of 0.3.

Although the adaptive beamformer algorithm is used as the source reconstruction algorithm throughout this study, we show the results of attempting to compute the resolution using the sLORETA algorithm[13] for comparison.

---

[3] Throughout this paper, the SNR is defined as the ratio between the square root of the power of the generated signal magnetic field and the square root of the power of the noise, which is 50 fT.

Plots of the hit rate, the false-detection rate, and A-prime with respect to the inter-source distance, obtained using sLORETA, are shown in Fig. 5. Here, the source intensity is set to 400 nAm, which corresponds to an SNR of 20. This figure shows that, even when the SNR is very high, the A-prime plot never reaches 0.75, and the spatial resolution is not defined under the definition used in this paper.

By repeating the Monte Carlo experiments with different source intensities, a plot of resolution with respect to source intensity can be obtained. Such a plot obtained with an array of 160 sensors is shown in Fig. 6. Here, the relationship between mean SNR and source intensity is shown in the lower panel. The source intensity is varied from 4 to 400 nAm. This range corresponds to the SNR range of approximately 0.2 to 20, which is the range encountered in most of MEG measurements. In Fig. 6, we can see that the resolution is approximately 3 cm for this sensor system when the source intensity is 20 nAm, which gives an SNR of 1. At a very high SNR ratio such as 20, the resolution becomes as small as 1 cm.

Figure 6 indicates that, for the source intensity range between 10 and 100 nAm, the plot of resolution can be regressed by a linear regression model:

$$\widehat{y}(I) = a(\log_{10} I) + b, \tag{7}$$

where I indicates the source intensity, and $\widehat{y}(I)$ indicates the modeled resolution (cm) at the source intensity I. The regression coefficients are obtained by least-squares fitting to data between 10 and 100 nAm, giving $a = -3.0$, and $b = 7.4$. The regression results are shown by the broken line in Fig. 6. The results indicate that increasing SNR by an order of magnitude improves resolution by 3 cm. In other words, a 3-cm improvement in resolution arises from a 10-fold improvement in SNR.

Note that the linear regression mentioned above was performed for the data in range of 10 and 100 nAm. The source intensity range from 10 to 100 nAm corresponds to the SNR range between 0.5 and 5 according to the bottom panel in Fig. 6. This range of SNR is most often encountered in MEG measurements, and thus it is referred to as the practical SNR range in this paper.

3.2 Dependence of resolution on the number of sensors

We next investigate how the resolution of neuromagnetic imaging systems depends on the number of sensors. Plots of resolution for the four types of sensor arrays in Fig. 2 are shown in Fig. 7(a). The plots in Fig. 7(a) show a general tendency toward improved resolution when the number of sensors is increased. Although the difference in resolution becomes small under high SNR conditions, there are clear improvements in resolution for the source intensity from 10 to 100 nAm, which corresponds to the SNR range between 0.5 and 5, the practical range of SNR.

To derive a clear quantitative relationship between resolution and number of sensors, we remove the dependence of resolution on source intensity. To do so, the resolution is standardized by that of the 160-sensor array. Let us define the standardized resolution of a k-sensor system at the source intensity I as $x_{(k)}(I)$. The value of $x_{(k)}(I)$ is computed using $x_{(k)}(I) = y_{(k)}(I)/y_{(k=160)}(I)$, where $y_{(k)}(I)$ is the resolution of a k-sensor system at source intensity I. We then apply the linear regression analysis to the standardized resolution data $x_{(k)}(I)$. That is, we use:

$$\widehat{x}_{(k)}(I) = a(k)(\log_{10} I) + b(k), \tag{8}$$

where $\widehat{x}_{(k)}(I)$ is the modeled standardized resolution computed using the above equation.

The results of the linear regression are shown by broken lines in Fig. 7(b). Here, we see that the dependence of the standardized resolution on source intensity becomes very small but the dependence is not completely removed. We thus further average the standardized resolution over the practical SNR range, such that

$$\beta(k) = \langle \widehat{x}_{(k)}(I) \rangle_{10 \leq I \leq 100}, \tag{9}$$

where $\langle \cdot \rangle_A$ indicates the average over the region $I \in A$. This mean value of $\beta(k)$, referred to as the effective standardized resolution, is considered to represent the standardized resolution for a sensor system under assessment.

The plot of the effective standardized resolution, $\beta(k)$, with respect to the number of sensors k is shown in Fig. 8. The plot shows that there is a relationship between $\log k$ and $\beta(k)$ that is approximately linear when k is less than 300. However, when k becomes greater than 300, the plot starts to deviate from the linear relationship.

We therefore apply a second-order regression model to this plot and the regression results are shown by the broken line in Fig. 8; the model fitted to the plot is expressed as

$$\widehat{\beta}(k) = 0.37(\log_{10} k)^2 - 2.2 \log_{10} k + 4.05, \tag{10}$$

where $\widehat{\beta}(k)$ is the modeled effective standardized resolution. The resolution for a given number of sensors can be predicted using Eq. (10). For example, this equation gives $\widehat{\beta}(64) = 1.28$ and $\widehat{\beta}(320) = 0.86$, so the increase in the number of sensors from 64 to 320 attains a 50% resolution improvements. However, it also gives $\widehat{\beta}(640) = 0.785$ and $\widehat{\beta}(1000) = 0.774$. The results indicate that, even if we increase the number of sensors from 640 to 1000, the improvement in the resolution is only 1%.

3.3 Resolution dependence on the helmet radius

The analysis described so far assumes that sensors are arranged on a surface of a spherical helmet with a 13 cm radius. Existing SQUID-based whole-head sensor systems have values more or less similar to 13 cm for the radius of their helmets, although their helmets are not exactly spherical. Requirements for the thickness of the helium dewar wall may result in similar helmet sizes. However, due to the recent development of non-SQUID-type room temperature sensors, it may be possible to develop a whole-head sensor system with a helmet having a much smaller radius. Therefore, the dependence of resolution on helmet size is next investigated.

We compute the resolution of arrays with 80, 160, 320, and 640 sensors for helmet radii of 11.5 cm and 10 cm. (The resolution for the helmet radius of 13 cm was computed, and the results are shown in Fig. 7.) In Fig. 9, the plots for the 160-sensor system are selectively shown. A general tendency for a smaller helmet system to give better resolution can clearly be seen in this figure.

The resolution values are then standardized by using the values of the 160-sensor system with the helmet size of 13 cm. That is, defining the raw resolution value of the k-sensor system and the helmet size of R as $y_{(k,R)}(I)$, the standardized resolution is computed using

$$x_{(k,R)}(I) = y_{(k,R)}(I)/y_{(k=160,R=13)}(I). \tag{11}$$

The same linear regression analysis as described in the preceding subsection is applied to $x_{(k,R)}(I)$ to derive the modeled standardized resolution $\widehat{x}_{(k,R)}(I)$. Figure 10 shows the raw resolution plots for 80-, 160-, 320-, and 640-sensor arrays in the top panels. The bottom panels show the results of the modeled standardized resolution analysis.

We next derive the effective standardized resolution $\beta(k,R)$ by using $\beta(k,R) = \langle \widehat{x}_{(k,R)}(I) \rangle_{10 \le I \le 100}$. The effective standardized resolution is plotted with respect to the number of sensors in Fig. 11. Here, the effective standardized resolution for the each of the three helmet sizes is plotted. The observation that these three plots are nearly parallel suggests that the resolution improvement due to the use of a smaller helmet is nearly independent from the number of sensors. To check this point, the effective resolution $\beta(k,R)$ is further normalized by the corresponding value when the helmet size is 13 cm. That is, the normalized effective resolution, $\bar{\beta}(k,R)$, is obtained by using $\bar{\beta}(k,R) = \beta(k,R)/\beta(k,R=13)$, and the results are shown in Table I.

The results in Table I were analyzed by two-way analysis of variance (2D-ANOVA) with the level of significance set to 0.005. The analysis indicates that the dependence of $\bar{\beta}(k,R)$ on the number of sensors k is not statistically significant but the dependence on helmet radius R is statistically significant. Therefore, the mean values obtained by averaging $\bar{\beta}(k,R)$ over k should represent the dependence of resolution on helmet size. Table I shows that, compared to the case of the 13-cm helmet, nearly 20% and 35% resolution increases are respectively attained if we use sensor helmets with radii of 11.5 cm and 10 cm.

Table I Normalized effective resolution $\bar{\beta}(k,R)$.

	number of sensors, k				
helmet radius R (cm)	80	160	320	640	mean
13	1	1	1	1	1
11.5	0.83	0.79	0.85	0.78	0.81
10	0.67	0.63	0.65	0.64	0.65

3.4 Resolution dependence on gradiometer baseline

We assess the effects of gradiometer baseline on resolution. Note that an axial gradiometer with a baseline of 5 cm has been assumed in our analysis presented so far. We here compute the resolution of 80-, 160-, 320-, and 640-sensor systems with axial gradiometers baseline B of 1.6 cm, 3.2 cm, 5.0 cm, and ∞[4] cm. Results are shown in Fig. 12. Here, the helmet radius is fixed at 13 cm. In this figure, we can observe a general tendency for a sensor system with a larger baseline to give a better resolution.

To make quantitative assessments on this tendency, we analyze the effective standardized resolution, i.e., we standardize each resolution value by using the corresponding resolution value when the baseline is 5 cm, and apply the linear regression analysis to obtain the effective standardized resolution. The results are shown in Table II.

We analyzed the results in Table II by 2D-ANOVA with the level of significance set to 0.005. The analysis indicates that the dependence on number of sensors k is not statistically significant but the dependence on the baseline value B is statistically significant. The mean values of the effective resolution across k thus show the dependence of the resolution on the baseline values. According to Table II, it can be seen that, compared to the 5 cm baseline case, 34% and 11% resolution losses occur if we use gradiometers with 1.6 cm and 3.2 cm baselines, respectively. On the other hand, use of a gradiometer with 5 cm baseline causes only 10% loss of spatial resolution, compared to the use of a magnetometer sensor.

Table II Effective standardized resolution for four values of gradiometer baseline.

	baseline (cm)			
number of sensors	1.6	3.2	5	∞
80	1.28	1.06	1.00	0.84
160	1.37	1.14	1.00	0.91
320	1.33	1.12	1.00	0.96
640	1.39	1.09	1.00	0.91
mean	1.34	1.10	1.00	0.90

3.5 comparison between planar and axial gradiometer arrays

We here assess the resolution of planar gradiometer arrays, and compare the resolution with that of axial gradiometer arrays. To do so, we define three orthogonal directions $(\boldsymbol{e}, \boldsymbol{f}, \boldsymbol{g})$ as shown in Fig. 13. The radial direction is defined as the $\boldsymbol{e}$ direction, and the two tangential directions are defined as the $\boldsymbol{f}$ and $\boldsymbol{g}$ directions in which $\boldsymbol{f}$ and $\boldsymbol{g}$ indicate the longitudinal and latitudinal directions, respectively.

---

[4] A gradiometer with $B = \infty$ indicates the magnetometer.

The planar gradiometer in which the two sensors are aligned in the longitudinal direction is referred to as the f-gradiometer, and the planar gradiometer in which the two sensors are aligned in the latitudinal direction is referred to as the g-gradiometer. We also assess the resolution of an "orthogonal gradiometer", which has a pair of the f and g gradiometers at the same location. (Note that the orthogonal gradiometer configuration is used in Elekta-Neuromag TRIUX$^{\mathrm{TM}}$.) Since a planar gradiometer with a large baseline is physically infeasible, we assess planer gradiometers with a 1.6 cm baseline and with a 3.2 cm baseline.

We compute the resolution of the f-gradiometer array, g-gradiometer array, and orthogonal gradiometer array. The sensor locations are the same as those of the axial 160-sensor array with a 13 cm helmet radius. Thus, the number of sensors is 160 for the f- and g-gradiometer arrays, and 320 for the orthogonal gradiometer array. The results of computing resolution are shown in Fig. 14. The results for the 1.6 cm baseline case are shown in the top panel and those for the 3.2 cm baseline case are shown in the bottom panel. The results for the 160 and 320 axial gradiometer arrays with the same baselines are also shown for comparison.

The results in Fig. 14 show that, although the axial gradiometer arrays have resolution significantly better than that of the f-gradiometer alone array and g-gradiometer alone array, the resolution for the orthogonal gradiometer array is better than that of the axial 160 gradiometer array. However, for a fair comparison, the orthogonal gradiometer array should be compared to the axial 320 gradiometer array, whose results are shown by the broken lines. It can be seen that the resolution of the orthogonal gradiometer array is very close to that of the 320 axial gradiometer array, and this indicates that the performance of the planar and the axial gradiometer arrays with the same baseline is nearly equal when we use the orthogonal gradiometer configuration.

3.6 Effects of vector field measurements on resolution

We here assess the effects of vector field measurements on resolution. The directions defined by the vectors $(\boldsymbol{e}, \boldsymbol{f}, \boldsymbol{g})$ are again used, and sensors that measures the magnetic field in the $\boldsymbol{f}$ and $\boldsymbol{g}$ directions are respectively referred to as the f- and g-sensors. The sensors that measure the magnetic field in the radial $(\boldsymbol{e})$ direction are referred to as the radial sensors, which have been considered in the preceding subsections. The sensors that measure the magnetic field in the all three $(\boldsymbol{e}, \boldsymbol{f}, \boldsymbol{g})$ directions are referred to as the vector sensors.

We compute resolution of four types of sensor arrays: the radial sensor array, the f sensor array, the g sensor array, and the vector sensor array. Here, all types of sensors are assumed to be magnetometers, and the sensors are arranged on a spherical helmet with a 13 cm radius. The sensor locations are the same as those of the 160 sensor array, and thus the number of sensors is 160 for all types of sensor arrays except the vector sensor array, which has 480 (160×3) sensors.

The resolution plots for these four types of sensor arrays are shown in Fig. 15. It can be seen in this figure that the resolution of the radial sensor array is significantly better than that of the two types of tangential sensor arrays. Although the vector sensor array attains the highest resolution, the difference between the vector and the radial sensor arrays is small.

To quantitatively assess the resolution differences among these sensor arrays, we apply the standardized resolution analysis where the resolution is standardized using the corresponding values of the radial sensor array. The results of computing the modeled standardized resolution are shown in Fig. 16(a). We then compute the effective resolution by averaging the modeled standardized resolution between I=10 and 100 nAm. Let us define the effective resolution for the radial, f-sensor, g-sensor, and vector sensor arrays as $\beta_{\rm rad}$, β_f, β_g, and $\beta_{\rm vec}$, respectively. The results of computing these effective resolution are given in the first line of Table 3. These results indicate that, compared to the use of the radial sensor array, an 80% and 40% resolution losses arise when the f- and g-sensor arrays are used. The use of the vector sensor array can attain 15% better resolution.

Table III Results of computing effective standardized resolution for radial, tangential, and vector sensor arrays[5]

	type of sensors			
sensor arrangement	$\beta_{\rm rad}$	β_f	β_g	$\beta_{\rm vec}$
type I	1	1.8	1.4	0.85
type II	1	2.4	1.8	0.91

The computer simulation described so far uses the assumption that the radial and tangential sensors are aligned on the same sphere surface with a 13 cm radius. This assumption is somewhat unrealistic for the tangential sensors. Typical sensors in existing MEG arrays are coils with a 2–3 cm diameter. If we use such coils for the tangential sensors, the center of the coil should be arranged 1–1.5 cm above the surface of the helmet. Namely, the tangential sensor array should use a helmet with a radius at least 1 cm larger than the radius of the helmet used for the radial sensor array. This fact should be taken into account when we compare performance between the radial and tangential sensor arrays.

We compute the resolution assuming that the tangential sensors are arranged on a sphere with a radius of 14 cm. The results of computing the modeled standardized resolution in this case are shown in Fig. 16(b), and the results of computing the effective resolution are given in the second line of Table III. These results indicate that the resolution difference between the radial and tangential sensor arrays is as large as 80% for the g-sensor array and 140% for the f-sensor array. The resolution improvements due to the use of the vector sensor array is less than 10%, despite the vector sensor array uses 3 times more sensors such as 480 sensors in the case of the study described here.

---

[5] In this table, Type I sensor arrangement indicates that all types of sensors are arranged on a sphere with a 13 cm radius. Type II sensor arrangement indicates that the radial sensors are arranged on a sphere with a 13 cm radius but the tangential sensors are arranged on a sphere with a 14 cm radius.

3.7 Resolution of existing sensor arrays

We compute the resolution of two types of existing neuromagnetic imaging systems: MEGvision$^{\mathrm{TM}}$ (Yokogawa Electric Corporation, Tokyo, Japan) and Elekta-Neuromag TRIUX$^{\mathrm{TM}}$. MEGvision$^{\mathrm{TM}}$ has 160 axial gradiometers with a 5 cm baseline[14], and Elekta-Neuromag TRIUX$^{\mathrm{TM}}$ has a total of 306 sensors consisting of 102 orthogonal planer gradiometers and 102 magnetometers[15]. Both systems have sensors arranged on a helmet-shaped surface with a radius of approximately 13 cm, although their helmets are not exactly spherical.

The results of computing resolution-source-intensity-SNR plots are shown in Fig. 17. Here, to compute SNR, the sensor noise with a standard deviation of 50 fT is again assumed. Here, the plot labeled"Y" indicates the results from MEGvision$^{\mathrm{TM}}$. The plot labeled"El-G" indicates the results from TRIUX in which only the planar gradiometer sensors are used, and the plot labeled "El-G+M" indicates the plot from TRIUX in which both the planar gradiometer and magnetometer sensors are used. The range of the source intensity from 4 to 200 nAm corresponds to the SNR range from 0.3 to 15 for MEGvision$^{\mathrm{TM}}$ and 0.2 to 10 for Elekta-Neuromag TRIUX$^{\mathrm{TM}}$. The results in Fig. 17 show that the resolution of MEGvision$^{\mathrm{TM}}$ is almost the same as that of Elekta-Neuromag TRIUX$^{\mathrm{TM}}$. However, if only the planar gradiometers are used, the resolution of TRIUX$^{\mathrm{TM}}$ is significantly lower than that of MEGvision$^{\mathrm{TM}}$ in the practical SNR range.

4 Conclusions

This paper proposes a novel signal-detection-theory-based definition for the resolution of neuromagnetic imaging systems, and develops a Monte Carlo computer simulation method to compute the resolution. Using the resolution as a performance measure, various types of sensor hardware are compared. We first analyze the performance changes due to change in the number of sensors, and derive an empirical equation that expresses the relationship between resolution and number of sensors. We then analyze the influence of the sensor helmet size on resolution, and find that sensor helmets with radii of 11.5 cm and 10 cm, respectively, provide nearly 20% and 35% better resolution than the helmet with a 13 cm radius. We analyze the performance changes due to changes in gradiometer baseline and find that, compared with the 5 cm baseline case, 34% and 11% resolution losses are respectively caused if we use a gradiometer with a 1.6 cm or a 3.2 cm baselines. On the other hand, use of a gradiometer with a 5 cm baseline causes 10% loss of spatial resolution, compared to the use of a magnetometer sensor. We find that the planar and axial gradiometer systems attain almost the same resolution. We also compare performances between the radial and vector sensors, and find that, the resolution improvement due to the use of the vector sensor array is only 10–15 %. Finally, we compute the resolution of two markedly different existing MEG systems, MEGvision$^{\mathrm{TM}}$ (Yokogawa Electric Corporation, Tokyo, Japan) and Elekta-Neuromag TRIUX$^{\mathrm{TM}}$, (Elekta

Corporate, Stockholm, Sweden), and find that these two systems have almost the same resolution.

5 Acknowledgements

This work was supported by a Grant-in-Aid from the Japanese Ministry of Education, Culture, Sports, Science, and Technology (No 26282149) and by a grant from Konika-Minorta Corporation. The author is grateful to Ei HIyama and Ryo Koga for their dedication in data analysis.

A Appendix

A.1 Determination of voxel size

The voxel size V must be determined such that the voxel discretization does not cause additional inaccuracy in source detection. To explore how to determine V, let us consider four scenarios with different $\varDelta$ and V settings where $\varDelta$ is the inter-source distance. The scenarios are depicted as a one-dimensional model in Fig. 18(a)–(d) . Here, the locations of the two sources are indicated by filled squares, and voxels are indicated by filled circles. The voxels neighboring the sources are labeled as “A”, “B”, “C”, and “D”. Here, we assume that an ideal reconstruction is performed with no source localization bias and no blur, that is, only the voxel nearest a source location has a reconstructed source power (indicated by a vertical arrow) due to that source. Other voxels have no source power and their voxel values are zero.

In Fig. 18(a), a case where V is greater than $\varDelta/2$ is shown. In this case, two voxels can exist between the two sources, such voxels are labeled“B” and “C” in the figure. Voxel “B” is the voxel nearest Source 1 and has a reconstructed power due to that source. Also, voxel “C” is the voxel nearest Source 2 and has a reconstructed power due to that source. As a result, there is only a single local peak either at voxel“B” or at voxel “C” and the two sources are not resolved in the reconstructed image.

Figure 18(b) shows a case where the voxel size V is equal to $\varDelta/2$. In this figure, the voxel nearest Source 1 is voxel “A”, which has a power due to this source. The voxel nearest Source 2 is voxel “C”, which has a power due to this source. As a result, two local peaks exist at voxels“A” and “C”, and the two sources are resolved. However, there is a “worst case scenario”, which is shown in Figure 18(c). In this scenario, the two sources are exactly at the midpoint of two voxels. That is, Source 1 is located at the midpoint between voxel “A” and voxel “B”, and it is equally possible that voxel “A” has a reconstructed source power or that voxel “B” has the reconstructed power. Figure 18(c) shows a case where voxel “B” has the power from Source 1 and voxel “C has the power from Source 2. In such a case, there is a single local peak either at voxel “B” or at voxel “C”, and the two sources are not resolved.

Finally, a case where the voxel size is smaller than $\mathit{\Delta}/2$ is shown in Figure 18(d), in which Source 2 is still located at the midpoint between voxels "C" and "D" and the voxel nearest Source 1 is voxel "A". Therefore, we have local peaks at voxel "A" and voxel "C", and the two sources are resolved. The one-dimensional analysis described above indicates that, to avoid voxel discretization errors in local peak detection, the voxel size V should be smaller than half of the inter-source distance $\mathit{\Delta}$.

The arguments above are extended to three-dimensions. A three-dimensional source-and-voxel configuration, corresponding to the one-dimensional case in Fig. 18(c), is shown in Fig. 18(e). In this figure, the two sources are located at the center of the cubic grid of voxels, and an empty cube exists between the two cubes containing the sources. The inter-source distance between the two sources $\mathit{\Delta}$ is equal to $2\sqrt{3}V$. The above arguments for the one-dimensional case indicate that the voxel size V should be determined to satisfy

$$V < \frac{\mathit{\Delta}}{2\sqrt{3}} = 0.28\mathit{\Delta}. \tag{12}$$

In our Monte Carlo simulation, the voxel size is set to $0.2\mathit{\Delta}$ when $\mathit{\Delta} \leq 2.5$ cm, and it is set to 0.5 cm when $\mathit{\Delta} > 2.5$ cm.

A.2 Determination of detection radius D

We next determine the detection radius D. Figure 19(a) shows the three-dimensional voxel cubic grid with a source located inside the cube. Under the ideal assumption that the reconstruction has no localization bias and no blur, the voxel closest to the source has a reconstructed source power. If the source exists at exactly the center of the cube, the eight voxels at the vertices have an equal probability of having a reconstructed power. In this case, the distance between the source and one of the voxels, denoted X in Fig. 19(a), is equal to $\sqrt{3}V/2$. Therefore, the detection radius D must be greater than $\sqrt{3}V/2$, because if $D < \sqrt{3}V/2$ the reconstructed source may not be counted as a "detected source", even when the ideal reconstruction is performed.

We next determine the upper limit of D. If we set a large value to D, wrong reconstruction may be counted as a correct detection. To avoid such possibilities, D should be determined so as not to include voxels belonging to adjacent cubes. In Fig. 19(b), two neighboring cubic grids of voxels are shown and a source is located at the center of the lower cube. In this figure, the voxel nearest the source but belonging to the upper cube is marked by a triangle. The distance between this voxel and the source is denoted Y, which is equal to $\sqrt{11}V/2$. Therefore, to exclude this voxel, D should satisfy the relationship,

$$\frac{\sqrt{3}}{2}V \approx 0.87V < D < \frac{\sqrt{11}}{2}V \approx 1.66V. \tag{13}$$

In our Monte Carlo simulation, we use the value $D = 1.5V$ for the detection radius.

A.3 Derivation of Eq. (6)

A-prime is defined as the area under the ROC curve[9]. The first-order approximation of this area is the area of a rectangle whose corners have coordinates defined by $(0,0)$, (F,H), $(1,1)$, and $(1,0)$, as shown in Fig. 20. Thus, the first-order approximation of the A-prime metric is expressed as

$$A_p = \frac{HF + (H+1)(1-F)}{2} = \frac{H-F}{2} + \frac{1}{2}, \tag{14}$$

which is Eq. (6).

References

[1] M. Hämäläinen, R. Hari, R. J. Ilmoniemi, J. Knuutila, and O. V. Lounasmaa, "Magnetoencephalography-theory, instrumentation, and applications to noninvasive studies of the working human brain," *Rev. Mod. Phys.*, vol. 65, pp. 413–497, 1993.

[2] S. Supek and C. J. Aine, *Magnetoencephalography: From Signals to Dynamic Cortical Networks.* Springer, 2014.

[3] K. Sekihara and S. S. Nagarajan, *Electromagnetic Brain Imaging: A Bayesian Perspective.* Springer, 2015.

[4] K. Sekihara and S. S. Nagarajan, *Adaptive spatial filters for electromagnetic brain imaging.* Berlin, Heidelber: Springer-Verlag, 2008.

[5] S. Baillet, J. C. Mosher, and R. M. Leahy, "Electromagnetic brain mapping," *IEEE Signal Processing Magazine*, vol. 18, pp. 14–30, 2001.

[6] J. Nenonen, S. Taulu, M. Kajola, and A. Ahonen, "Total information extracted from MEG measurements," in *International Congress Series*, vol. 1300, pp. 245–248, Elsevier, 2007.

[7] J. Sarvas, "Basic mathematical and electromagnetic concepts of the biomagnetic inverse problem," *Phys. Med. Biol.*, vol. 32, pp. 11–22, 1987.

[8] B. D. Van Veen, W. Van Drongelen, M. Yuchtman, and A. Suzuki, "Localization of brain electrical activity via linearly constrained minimum variance spatial filtering," *IEEE Trans. Biomed. Eng.*, vol. 44, pp. 867–880, 1997.

[9] J. Snodgrass and J. Corwin, "Pragmatics of measuring recognition memory: applications to dementia and amnesia," *J. Exp. Psychol. Gen.*, vol. 117, pp. 34–50, 1988.

[10] J. P. Owen, D. P. Wipf, H. T. Attias, K. Sekihara, and S. S. Nagarajan, "Performance evaluation of the champagne source reconstruction algorithm on simulated and real M/EEG data.," *NeuroImage*, vol. 60, pp. 305–23, 2012.

[11] D. P. Wipf, J. P. Owen, H. T. Attias, K. Sekihara, and S. S. Nagarajan, "Robust Bayesian estimation of the location, orientation, and time course of multiple correlated neural sources using MEG," *NeuroImage*, vol. 49, pp. 641–655, 2010.

[12] J. M. Zumer, H. T. Attias, K. Sekihara, and S. S. Nagarajan, "A probabilistic algorithm integrating source localization and noise suppression for MEG and EEG data," *NeuroImage*, vol. 37, pp. 102–15, 2007.

[13] R. D. Pascual-Marqui, "Standardized low resolution brain electromagnetic tomography (sLORETA): technical details," *Methods and Findings in Experimental and Clinical Pharmacology*, vol. 24, pp. 5–12, 2002.

[14] G. Uehara, Y. Adachi, J. Kawai, M. Shimogawara, M. Higuchi, Y. Haruta, H. Ogata, and H. Kado, "Multi-channel SQUID systems for biomagnetic measurement," *IEICE Trans. on Electronics*, vol. E86-C, pp. 43–54, 2003.

[15] "http://www.elekta.com/healthcare-professionals/products/elekta-neuroscience/functional-mapping/elekta-neuromag-product-specifications.html."

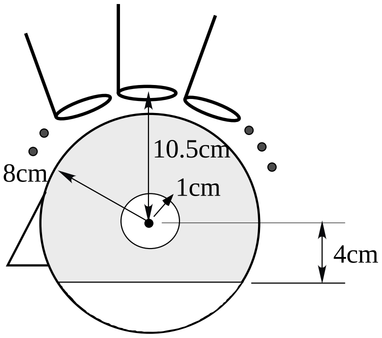

Figure 1: Simulated brain region assumed for Monte Carlo computer simulation. The center of the brain region is 10.5 cm below the sensor located at the center of the sensor array. A spherical-shell region with the outer radius of 8 cm and the inner radius of 1cm is defined as the brain region where the region more than 4 cm below the sphere center is excluded.

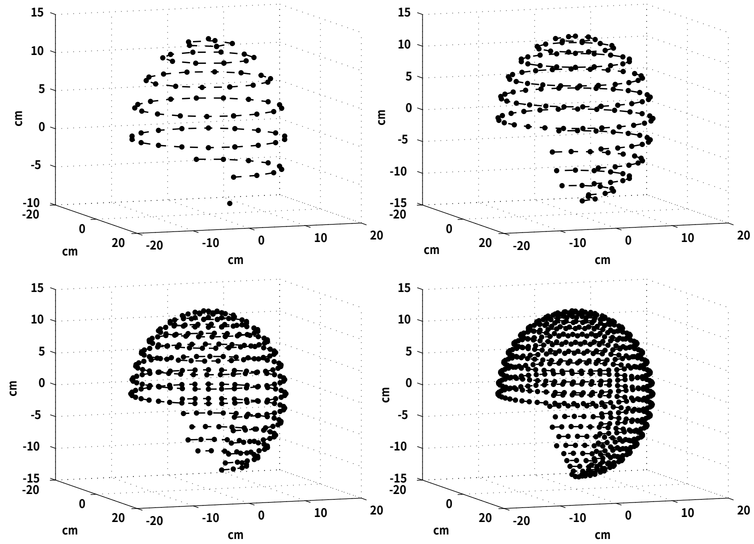

Figure 2: Four types of virtual whole-head sensor arrays with 80 sensors (top left), 160 sensors (top right), 320 sensors (bottom left), and 640 sensors (bottom right). The filled circles show the sensor locations. Sensors are arranged, with an equal inter-sensor spacing, on three-quoters of the surface of a spherical helmet having a 13 cm radius.

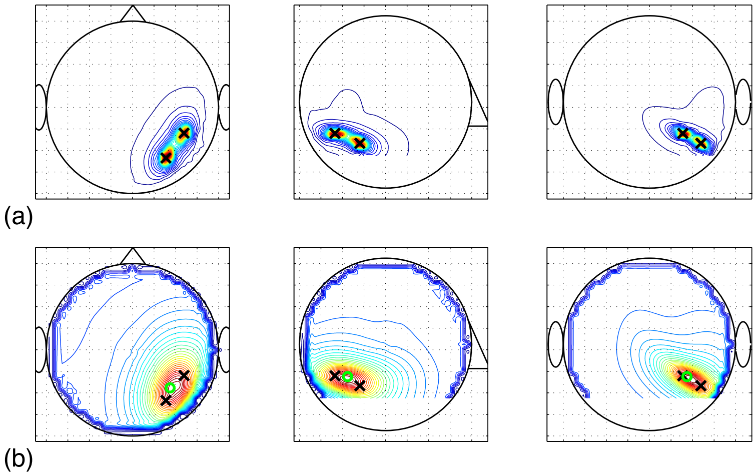

Figure 3: Two sets of examples of source reconstruction results where the two sources are 3 cm apart. Maximum intensity projections of the three-dimensional source power maps onto the transverse, sagittal, and coronal planes are shown, respectively, in the left, middle, and right panels. The contours indicate the relative power of the reconstructed sources. (a)A relatively high SNR case (SNR of 2) where the two sources are resolved. (b) A low SNR case (SNR of 0.5) where the two sources are not resolved. The crosses show the assumed locations of the two sources, and the blank circles in (b) show the location of a detected local peak.

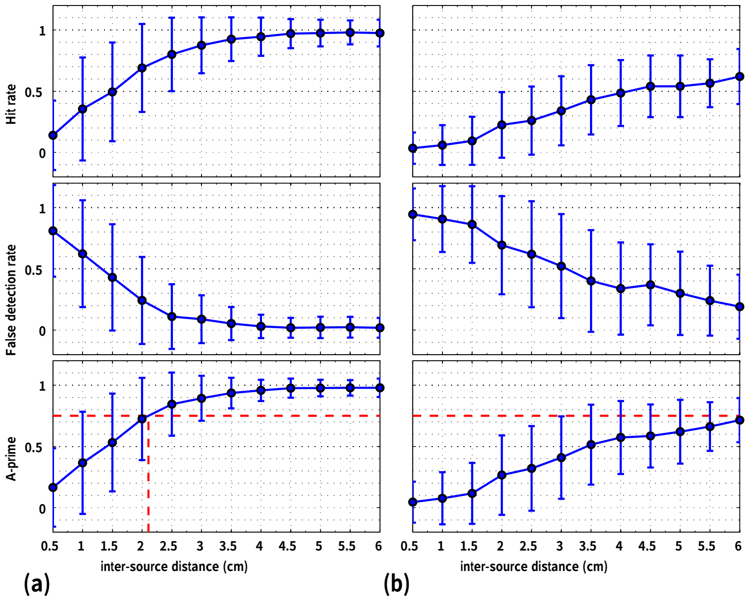

Figure 4: Plots of the hit rate (top), false detection rate (middle), and A-prime metric (bottom) with respect to the inter-source distance. These plots are obtained with the array of 160 sensors arranged on a spherical helmet with a 13 cm radius. (a) The source intensity is set to 60 nAm. (b) The source intensity is set to 6 nAm. The horizontal broken line in the A-prime plot shows the level of $A_p = 0.75$, and the vertical broken line shows the resolution determined as the inter-source distance that gives $A_p = 0.75$. The error bars indicate the 95% confidence interval.

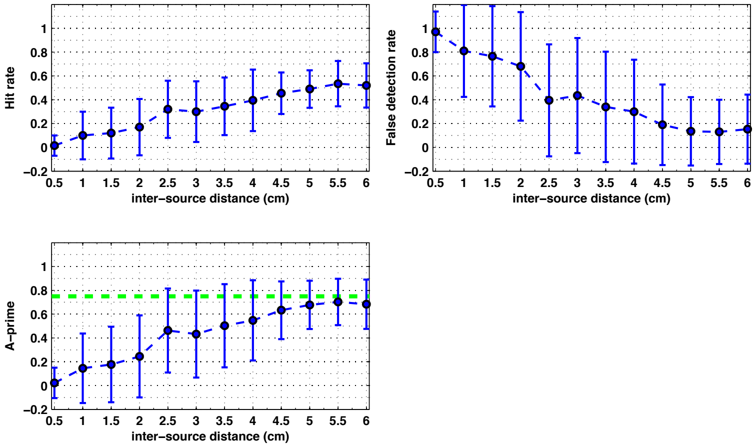

Figure 5: Plots of hit rate (top-left), false detection rate (top-right), and A-prime metric (bottom), with respect to the inter-source distance. These plots are obtained using sLORETA source reconstruction algorithm. The array of 160 sensors is used and the source intensity is set to 400 nAm, which corresponds to SNR of 20. The horizontal broken line in the A-prime plot shows the level of $A_p = 0.75$. The error bars indicate the 95% confidence interval.

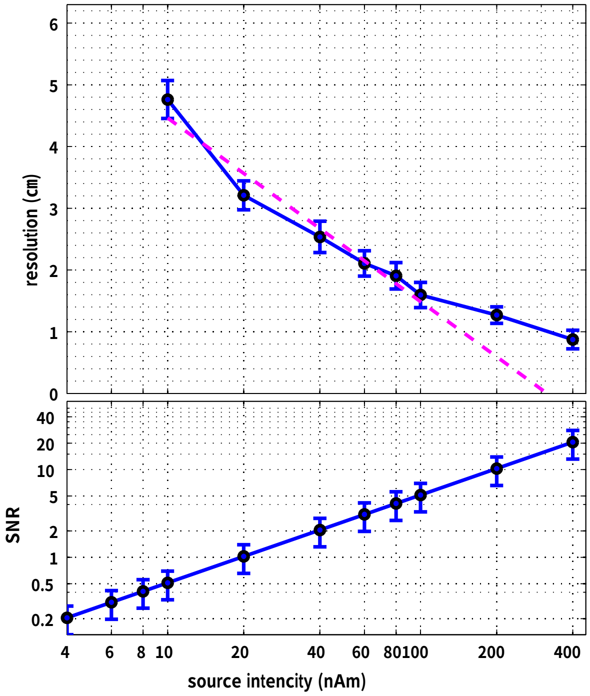

Figure 6: Resolution-source-intensity-SNR plot for the array of 160 sensors arranged on a sperical helmet with a 13 cm radius. The upper panel shows the plot of resolution versus source intensity and the lower panel shows the plot of SNR versus source intensity. The error bars indicates the 95% confidence interval. The broken line in the resolution plot indicates the regression results obtained using Eq. (7) fitted to the plot for the range of source intensity between 10 and 100 nAm.

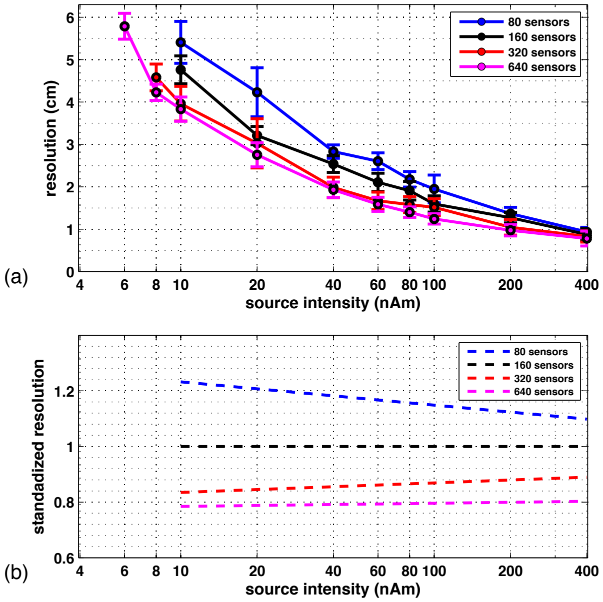

Figure 7: (a) Plots of resolution obtained using the four types of sensor arrays in Fig. 2. The error bars indicates the 95% confidence interval. (b) Plots of the modeled standardized resolution obtained using the regression analysis in Eq. (8).

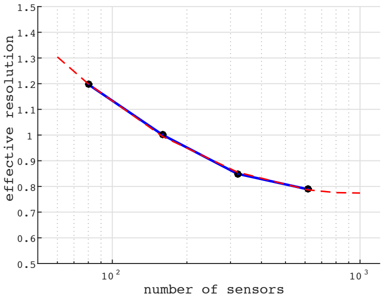

Figure 8: Plot of the effective standardized resolution, $\beta(k)$, with respect to the number of sensors k. The broken line indicates the line fitted by using the second-order regression model in Eq. (10).

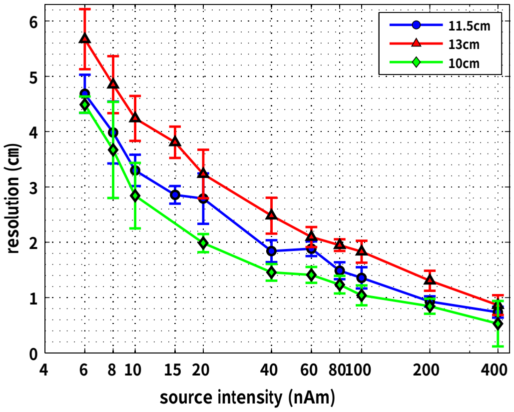

Figure 9: Plots of the resolution for the sensor system with 160 sensors for helmet sizes of 10, 11.5, and 13 cm. The plot for the 13 cm radius is the same plot as in Fig. 6.

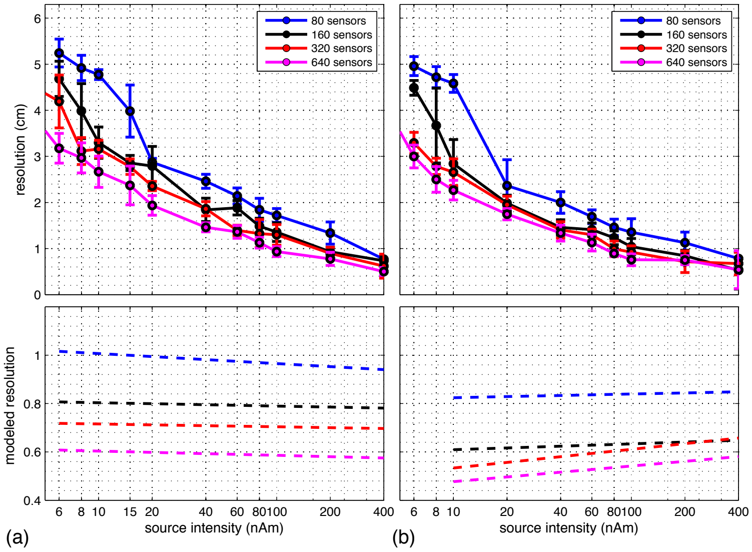

Figure 10: Plots of the resolution (top panel) and modeled standardized resolution $\widehat{x}_{(k)}(I)$ (bottom panel) for arrays of 80, 160, 320, and 640 sensors. (a) Helmet radius of 11.5 cm. (b) Helmet radius of 10 cm.

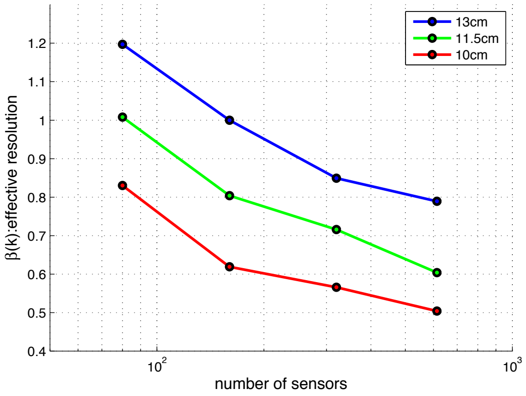

Figure 11: Plots of the effective standardized resolution $\beta(k)$ with respect to the number of sensors k for helmet sizes of 10, 11.5, and 13 cm. The plot for the helmet size of 13 cm is the same as that in Fig. 8.

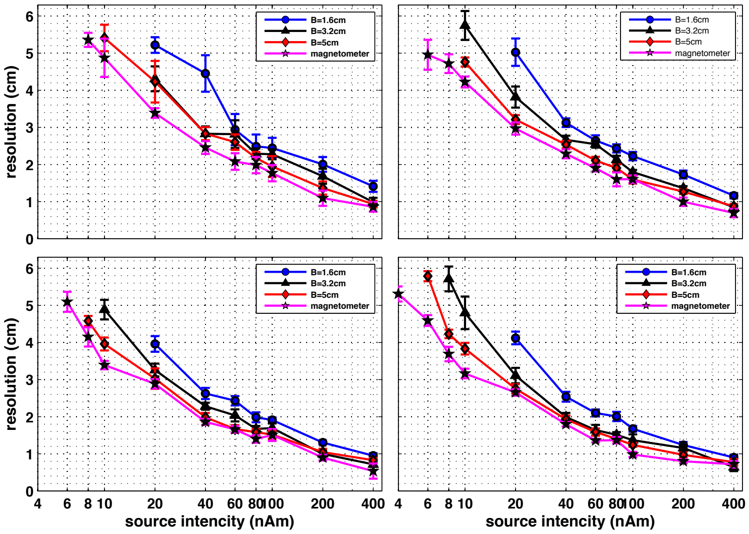

Figure 12: Resolution plot for the gradiometer baseline equal to 1.6, 3.2, 5, and ∞ cm. (The gradiometer with the baseline of ∞ cm indicates the magnetometer.) Results for the arrays with 80 sensors, 160 sensors, 320 sensors, and 640 sensors are respectively shown in the top-left, top-right, bottom-left, and bottom-right panels.

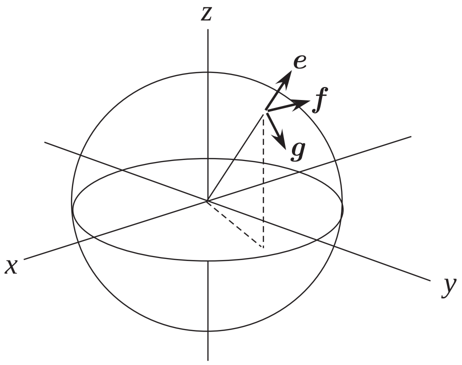

Figure 13: Schematic view of $(\boldsymbol{e}, \boldsymbol{f}, \boldsymbol{g})$ directions. The unit vector $\boldsymbol{e}$ represents the radial direction. The unit vectors $\boldsymbol{f}$ and $\boldsymbol{g}$ represent the two tangential directions, namely, the longitudinal and latitudinal directions.

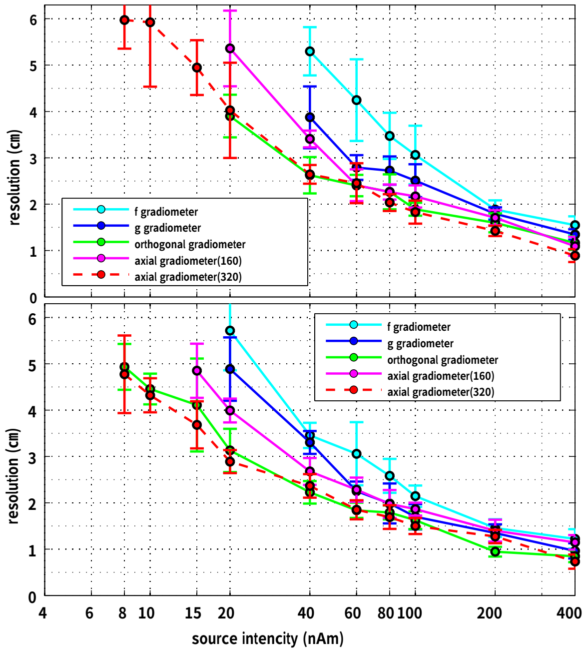

Figure 14: Plot of the resolution for the three-types of planar gradiometer arrays, as well as for the axial gradiometer arrays with the same baselines. The top panel shows results for gradiometer arrays with a 1.6 cm baseline and the bottom panel shows results for those with a 3.2 cm baseline. The sensor locations for the planar gradiometer arrays are the same as those of the axial gradiometer array with 160 sensors. The plot for the 320 axial gradiometer array is shown by the broken line. The sensors are arranged on a spherical helmet with a 13 cm radius.

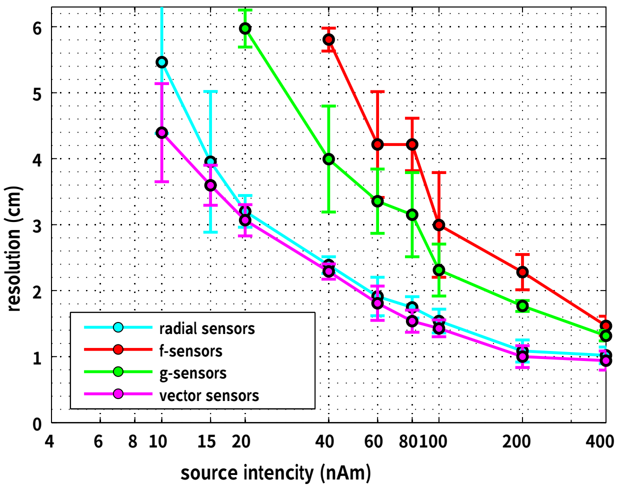

Figure 15: The plots of resolution versus source-intensity for the radial sensor array, the g sensor array, the f sensor array, and the vector sensor array. We assume that the sensor locations are the same as those for the 160 sensor array with a radius of 13 cm.

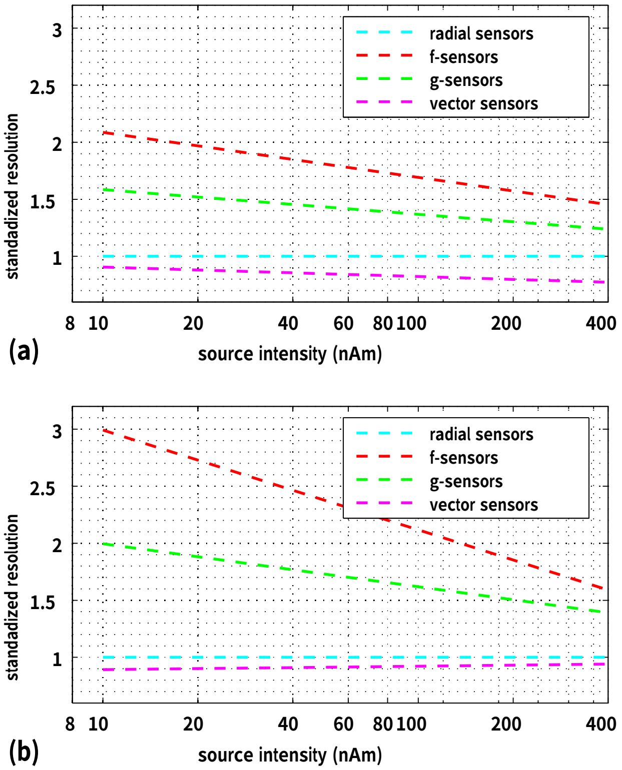

Figure 16: The plots of the modeled standardized resolution, $\widehat{x}_{(k)}(I)$, for the radial sensor array, the g-sensor array, the f-sensor array, and the vector sensor array. (a) Plots obtained under the assumption that the radial and the tangential sensors are aligned on the same spherical helmet with a 13 cm radius. (b) Plots obtained under the assumption that the radial sensors are aligned on a spherical helmet with a radius of 13 cm and tangential sensors on a spherical helmet with a radius of 14 cm.

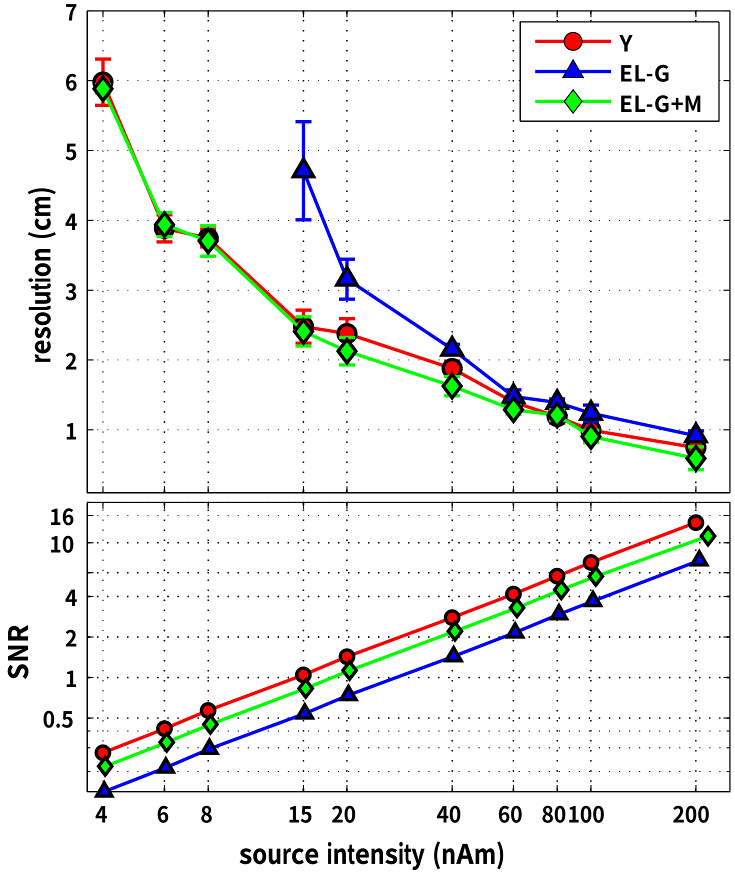

Figure 17: Plots of resolution and SNR versus source intensity for two existing sensor systems. The plot labeled "Y" indicates the results for MEGvision$^{\mathrm{TM}}$. The plot labeled by "El-G" indicates the results for TRIUX when only the planar gradiometer sensors are used. The plot labeled by "El-G+M" indicates the results for TRIUX when both gradiometer and magnetometer sensors are used. To compute SNR, we assume sensor noise with standard deviation of 50 fT.

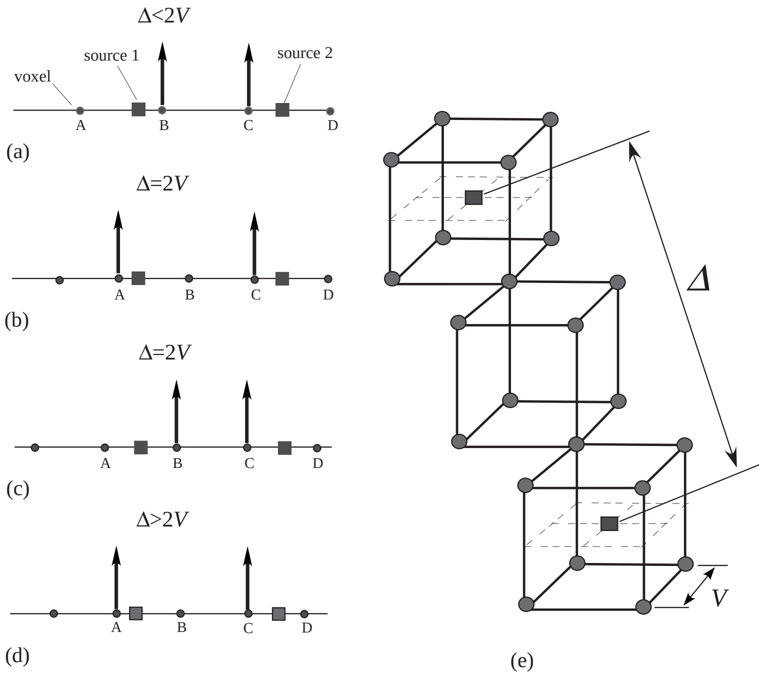

Figure 18: Four scenarios with different $\mathit{\Delta}$ and V settings are shown in (a)–(d) where $\mathit{\Delta}$ is the inter-source distance and V is the size of voxels. (a) A case where the voxel size is greater than $\mathit{\Delta}/2$. (b) A case where the voxel size is equal to $\mathit{\Delta}/2$ and the two sources can be detected. (c)A case where the voxel size is equal to $\mathit{\Delta}/2$ but the two sources cannot be detected. (d) A case where the voxel size is smaller than $\mathit{\Delta}/2$. The locations of the two sources are indicated by filled squares. Voxels are indicated by filled circles. The voxels neighboring the sources are labeled “A”, “B”, “C”, and “D”. (e) Three-dimensional source-and-voxel configuration corresponding to the one-dimensional case shown in (c). The two sources are located at the centers of the cubic grids of voxels, and an empty cube exists between the two cubes containing the sources.

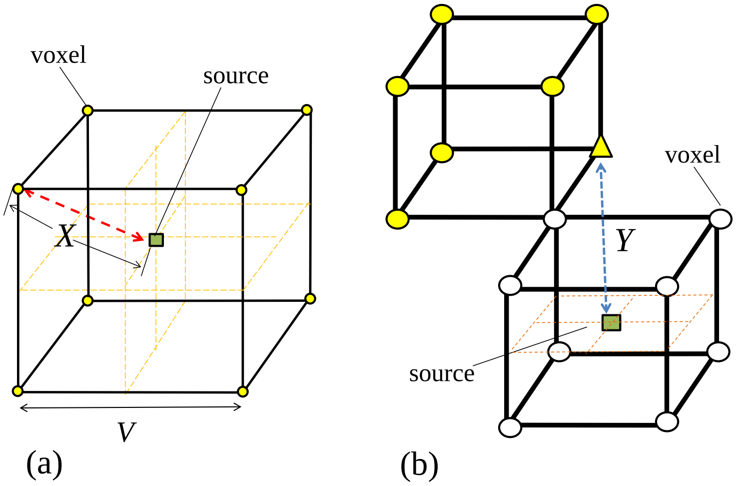

Figure 19: (a) Three-dimensional cubic grid of voxels with a source located inside the cube. The source location is indicated by a small rectangle. The distance between the source and one of the voxels is denoted X. (b) Two neighboring cubic grids of voxels with a source located at the center of the lower cube. The source location is indicated by a small rectangle. The voxel that is nearest the source but belongs to the upper cube is marked with a triangle, and the distance between this voxel and the source is demoted Y

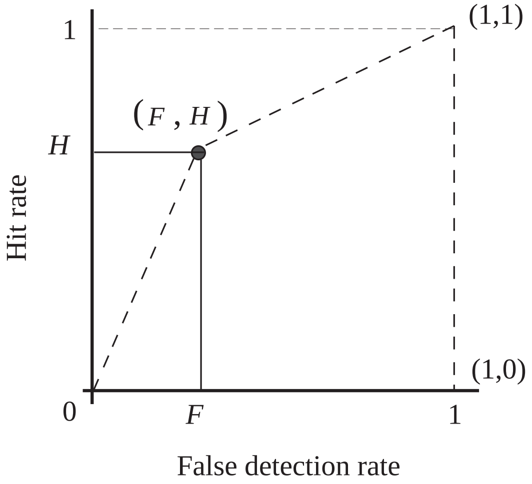

Figure 20: The concept of A-prime in which the area under the ROC curve is approximated by a rectangle whose corner's coordinates are defined by $(0, 0)$, (H, F), $(1, 1)$, and $(1, 0)$.